System Level Performance of Radar Waveforms

Ruixin Niu, Peter Willett, and Yaakov Bar-Shalom
Electrical and Systems Engineering Department
U-157, University of Connecticut
Storrs, CT 06269, USA

Abstract

It is well known that different radar signal waveforms produce very different resolution cells. These affect fine measurement error, gross measurement error through spurious sidelobe "pop-ups", and miss probability, and hence yield different tracking performance. In a recent paper, sonar waveform selection was explored via the hybrid conditional averaging (HYCA) method — a technique for evaluating the dynamic interaction between tracking and imperfect detection. Extension to the radar case is the subject of this paper, and this is more than evolutionary, since in order that range-rate measurements be available from resolution cells it is necessary that coherent processing of multiple pulses be used.

1 Introduction

Radar measurement and resolution performance, as well as target detection in clutter, depend strongly on the transmitted waveform. For example, constant frequency (CF) pulses yield good Doppler but poor delay resolution; and linearly frequency-modulated (LFM) transmitted waveforms have the opposite behavior. The choice of a suitable waveform is one of the more important problems of radar or sonar design, as the waveform controls resolution and clutter performance and also affects system cost.

The conventional approach to tracking system design has been to treat the sensor and tracking subsystems as completely separate entities: the two basic functions — automatic detection and tracking — are viewed and designed independently. Recently some authors have begun to investigate waveform selection problems from a system engineering point of view – see figure 1. In [Daum (1992)] the importance of waveform design from a tracking point of view is discussed. The author presents a comprehensive discussion of system considerations for multiple target tracking, including aspects of both measurement pattern optimization and waveform optimization. In [Kershaw and Evans (1997)] an adaptive waveform-selective probabilistic data association (WSPDA) algorithm for tracking a single target in clutter is presented. The assumption of an optimal receiver allows the inclusion of transmitted waveform specification parameters in the tracking subsystem equations, leading to a waveform selection scheme where the next transmitted waveform parameters are selected so as to minimize the average total mean-square tracking error at the next time step. This algorithm does not actually design the optimal waveform, but rather chooses the best from a set of allowable waveforms containing a number of classes.

In [Rago *et al.* (1998)] the authors explored the relationship between the pulse shape and the detection performance, and computed the corresponding measurement noise and state prediction covariance matrix, where the latter was derived via the algebraic Riccati Equation modified by the hybrid conditional averaging (HYCA) technique to account for missed detections. A number of observations were made, among the more important being that for a kinematic target

an *upsweep* linear frequency modulation (LFM) signal was superior to *downsweep* LFM and to constant frequency (CF) pulses due to the negative correlation between range and range-rate measurements. This is particularly so for low maneuvering-index targets.

In [Niu *et al.* (1999)] the analysis technique of [Rago *et al.* (1998)] was improved and augmented by adopting a consistent model of the resolution cell, and by incorporating the effect of false alarms. Thus:

- A probabilistic data association filter (PDAF) rather than a Kalman filter was assumed for tracking; hence both missed detections and false-alarms were accounted for.
- A realistic detection model was used: the effect of spurious detections caused by sidelobe "pop-ups" was incorporated.
- A "constant-volume" definition of the resolution cell was used; hence, it was possible to compare different waveforms in a consistent manner.
- A wide variety of waveforms was studied.

In order to obtain measurements for tracking, a practical consideration is that interrogation for targets' presence or absence is possible only at a grid of sampling points, and hence a resolution cell must arise. In [Rago *et al.* (1998)] these resolution cells were defined by probability of detection contours, and hence there was considerable variation in both size and shape, with the upshot that certain of the resulting plots were "choppy" in appearance. Those in [Niu *et al.* (1999)] are quite smooth; further, since the resolution cell was of constant volume – meaning that the computational load accruing from "sampling" was held fixed – a wider variety of waveform types could reasonably be studied and compared. In fact, a menu of CF, LFM, parabolic FM, XFM/VFM, coded pulses, and hybrids were explored.

The results in [Niu *et al.* (1999)] were limited to the sonar situation. The main reason for this, aside from the inherent interest of tracking underwater targets, was a reliance on *single-pulse* operation. Central to the analysis is an assumption that a target's true location is uniformly distributed within a range/range-rate resolution cell; in order that this be applicable to the radar case it is necessary either that (i) the pulse-length be unrealistically long (several milliseconds); or (ii) the radar frequency be unrealistically high (several hundred gigahertz); or (iii) the target's range-rate be unrealistically fast (Mach 10 or more). Without such assumptions it is not reasonable to assume uniformity; in fact, there is little reason for a target to escape from a zero-Doppler resolution cell. (Many radar systems [Daum (1992), Levanon (1988)] appear to operate in this way, with range-only measurements: Doppler appears only as a somewhat predictable perturbation about a true range measurement.)

With extension to a *multi*-pulse radar operating in a coherent mode [Scheer and Kurtz (1993)] the above objections become moot, since the effective pulse duration can become quite long. Thus, in this paper we extend analysis to the radar situation:

- It is assumed that the radar signal is operating in a multi-pulse mode.
- It is assumed that there is appropriate signal processing to avoid dilution of results from the "bed of nails" ambiguity function inherent to multi-pulse operation.
- The effect of the volume of resolution cell is explored.
- The effect of the number of pulses is explored.
- Both CF and LFM pulse trains, with Hamming and rectangular weighting, are studied.

- Both an "averaging" and "strongest return" approach to derivation of the measurement to be presented to the tracker from the resolution-cell-sampled returns are studied.

With respect to the second item above, the analysis of [Niu *et al.* (1999)] would have accorded a multiple-pulse waveform an unrealistically high measurement inaccuracy.

2 Modeling

2.1 Detection

Receiver processing is assumed, without loss of generality, to be performed at "baseband"; that is, subsequent to carrier-removal via mixing. If the transmitted baseband signal is $s(t)$, the matched filter is the one with an impulse response $h(t) = s^*(-t)$, i.e. the impulse response of the matched filter is the conjugate time-reversed baseband signal. With $r_i(t)$ the received waveform, and $r(t)$ the baseband representation of $r_i(t)$, we have, as an output process of our matched filter,

$$\begin{aligned} x(t) &= \int s^*(\lambda - t) r_i(\lambda) e^{-j2\pi f_0 \lambda} d\lambda \\ &\equiv \int s^*(\lambda - t) r(\lambda) d\lambda \end{aligned} \tag{1}$$

where f_0 is the carrier frequency, and $s(t)$ is a replica of the transmitted baseband signal.

The (baseband) received signal will be modeled as a return from a Swerling 1 target, meaning that we have [Levanon (1988)]

$$\begin{aligned} r(t) &= \left(\sum_i A_i \right) s(t, \tau, f_d) \mathcal{I}(target) + \nu(t) \\ &= A s(t - \tau) e^{j2\pi f_d t} \mathcal{I}(target) + \nu(t) \end{aligned} \tag{2}$$

where $s(t, \tau, f_d) = s(t - \tau) e^{j2\pi f_d t}$ is a delayed (τ) and Doppler-shifted (f_d) replica of the emitted baseband complex envelope signal $s(t)$, and $\mathcal{I}(target)$ is a target indicator. The complex numbers A_i represent the amplitude and phase of each of the target reflectors. For a Swerling 1 model the assumption is that there are many such reflectors, each one with a random amplitude and phase. Hence $A = \sum_i A_i$ approaches a complex Gaussian random variable with zero mean and variance $2\sigma_A^2$. [Levanon (1988)]. We assume $\nu(t)$ is complex white Gaussian noise independent of A, with zero mean and variance $2N_0$.

If the return signal is expected to be Doppler shifted by a frequency f_m and delayed by a time τ_m (the subscript m denotes "measured"), then the appropriate matched filter output is given by

$$x(\tau_m, f_m) = \int s^*(\lambda - \tau_m) e^{-j2\pi f_m (\lambda - \tau_m)} r(\lambda) d\lambda \tag{3}$$

and the appropriate test is of

$$|x(\tau_m, f_m)|^2 \tag{4}$$

against a threshold whose value is a function of the desired false alarm rate. This forms the basis of our analysis: we compute (4) at an appropriate grid of points in delay/Doppler (or range/range-rate) space, and use any threshold exceedances to estimate a target's coordinates.

2.2 The Ambiguity Function and the Measurement

Of major interest in the sequel is the "ambiguity function" [Levanon (1988)], given by

$$\mathcal{A}(\tau, f) = \frac{1}{\left(\int |s(\lambda)|^2 d\lambda\right)^2} \left| \int s(\lambda) s^*(\lambda - \tau) e^{j2\pi f \lambda} d\lambda \right|^2 \tag{5}$$

The ambiguity function specifies the output of the matched filter in the absence of noise; its shape is related to the implied resolution cell, and is strongly dependent on the waveform. The importance of the ambiguity function is that the response of the statistic (4) to a target having true delay τ_a, true Doppler shift f_a (the subscript a denotes "actual"), and normalized complex return amplitude A, is given by

$$|A|^2 \mathcal{A}(\tau_m - \tau_a, f_a - f_m) \tag{6}$$

plus a noise term which for reasonably large signal-to-noise ratios (SNRs) is insignificant. For the Swerling 1 target model, the multiplier $|A|^2$ has an exponential distribution. Perhaps more important, it is *the same for all* (τ_m, f_m) *pairs*. This means that a strong target return will cause many contiguous (and in the case of an ambiguity function with unfortunate sidelobes, some noncontiguous) matched-filter threshold exceedances; and that a weak target return will cause correspondingly few.

We now are interested in the ambiguity function of a pulse train. If the envelope of each pulse of unit energy is $s_n(t)$, then that of a train of N_p equally spaced pulses is

$$s(t) = \frac{1}{\sqrt{N_p}} \sum_{n=0}^{N_p - 1} s_n(t - nT_R) \tag{7}$$

where T_R is the pulse repetition period. In some implementations a "staggered" pulse repetition time [Scheer and Kurtz (1993)] is used to avoid ambiguity; we do not explore that here. The division by $\sqrt{N_p}$ will maintain unit energy for the entire train. For a uniform (that is, constant frequency) pulse train $s_n(t)$ is

$$s_n(t) \;=\; \begin{cases} 1 & 0 \le t < t_p \\ 0 & else \end{cases} \tag{8}$$

where t_p is the pulse length. For an LFM pulse train, we have $s_n(t)$ as

$$s_n(t) \;=\; \begin{cases} e^{jbt^2} & 0 \le t < t_p \\ 0 & else \end{cases} \tag{9}$$

The parameter b controls the LFM sweep-rate, the total frequency sweep being bt_p/π Hz in t_p seconds.

Ambiguity functions for these two kinds of pulse trains are shown in figures 2 and 3. The ambiguity functions have many replicas, and sometimes it is referred to as a "bed of nails". According to the techniques of [Niu *et al.* (1999)] all threshold exceedances from by all replicas would be averaged to obtain a measurement. This is not realistic: the posterior uncertainty from tracking can restrict attention to only one (primary) replica, and if this is not the case we argue that the target track is so inaccurate that it can be considered lost. At any rate, from [Levanon (1988)], we know the spacing between replica peaks is T_R in delay and $\frac{1}{T_R}$ in Doppler. We thus take as the "neighborhood" (see Assumption 1, below) the rectangles in figures 2 and 3. The borders along the delay and Doppler axes are $[-T_R/2\ T_R/2]$ and $[-\frac{1}{2T_R}\ \frac{1}{2T_R}]$, respectively.

Assumption 1 *Observations are exceedances of a threshold η by $\{|x(\tau_m, f_m)|^2\}$ within the rectangular neighborhood of dimension $T_R \times 1/T_R$ around the main peak, according to (4), at a grid of delay/Doppler-shift points $\{\tau_m, f_m\}$. If a target with complex return amplitude A is present at delay/Doppler-shift coordinates $\{\tau_a, f_a\}$, then threshold exceedances are directly computable from (6).*

The sampling in range and range-rate is illustrated in figure 4. Note that an alternative sampling, in which the resolution cell parallelograms were oriented such that range-rate sampling was fine and range sampling coarse, was explored in [Niu *et al.* (1999)], with the conclusion that there was little difference.

Assumption 2 *When there are contiguous or nearby threshold exceedances it is reasonable to take as the estimated target location their direct average.*

More generally a weighted average based upon the target return strengths may be preferable; however, in our experience to date this makes little difference. However, we later explore the situation that the *strongest* measurement is taken as true, with no averaging. Some model must be made for the target location, and it is reasonable to assume uniformity. The idea is illustrated in figure 5 and formalized in:

Assumption 3 *The actual target location (τ_a, f_a) has a uniform distribution within the resolution cell defined by the sampling grid. For a target whose actual location is in a "corner" of the resolution cell this may imply a high miss probability.*

As indicated earlier, it is to make this assumption reasonable with radar parameters that we must assume multi-pulse operation.

We have an expression for the measurement error covariance :

$$\mathbf{R}_m = \int_{\begin{pmatrix} r \\ v \end{pmatrix} \in \mathcal{R}} \int_\gamma \frac{1}{|\mathcal{R}|} \begin{pmatrix} \hat{r}(\gamma, r_a, v_a) - r_a \\ \hat{v}(\gamma, r_a, v_a) - v_a \end{pmatrix} \begin{pmatrix} \hat{r}(\gamma, r_a, v_a) - r_a \\ \hat{v}(\gamma, r_a, v_a) - v_a \end{pmatrix}^T p(\gamma) d\gamma dr_a dv_a \quad (10)$$

where γ refers to the magnitude square of the return, and $\mathcal{R}$ is the basic resolution cell having area $|\mathcal{R}|$. $p(\gamma)$ is the probability density function of γ. For a Swerling 1 model:

$$p(\gamma) = \frac{1}{1 + SNR} e^{-\gamma/(1+SNR)} \quad (11)$$

The estimates are formed as direct averages:

$$\hat{r}(\gamma, r_a, v_a) = \frac{\sum_{r_m, v_m} r_m \mathcal{I}(\gamma \mathcal{A}(\tau_m - \tau_a, f_a - f_m) \geq \eta)}{\sum_{r_m, v_m} \mathcal{I}(\gamma \mathcal{A}(\tau_m - \tau_a, f_a - f_m) \geq \eta)} \quad (12)$$

$$\hat{v}(\gamma, r_a, v_a) = \frac{\sum_{r_m, v_m} v_m \mathcal{I}(\gamma \mathcal{A}(\tau_m - \tau_a, f_a - f_m) \geq \eta)}{\sum_{r_m, v_m} \mathcal{I}(\gamma \mathcal{A}(\tau_m - \tau_a, f_a - f_m) \geq \eta)} \quad (13)$$

for which $\mathcal{I}$ denotes the indicator function. The integration over the resolution cell (i.e. over (r_a, v_a)) in (10) is performed via evaluation over a dense grid of 400 points uniformly spaced within the resolution cell; the integration over γ is explicit. The conversion from delay/Doppler to range/range-rate is well-known to be $r = (\tau c)/2$ and $v = -(cf_d)/(2f_0)$, with c the speed of propagation and f_0 the transmitted carrier frequency.

2.3 The Resolution Cell

What remains is the definition of the resolution cell $\mathcal{R}$ itself. Selection of $\mathcal{R}$ is to some extent a matter of choice; but it seems reasonable to set certain ground rules. These are: (i) that the resolution cell pattern form a tesselating grid; (ii) that the volume of the resolution cell is a function of N_p, and for a given N_p, the volume should be constant, regardless of its actual shape; and (iii) that the resolution cell be oriented and shaped to match, in some sense, the ambiguity function. While the first consideration could give rise to many different patterns, we adopt the convention that the resolution cell must be a parallelogram. The second rule avoids the problem in [Rago *et al.* (1998)], and further seems natural from consideration of fairness (all waveforms being examined imply the same sampling effort). Since this measure matches the case of a CF pulse, we initially ($\alpha = 1$) choose the area of the resolution cell (in (r_a, v_a)-space) as $(ct_p) \times (\frac{c}{f_0 N_p T_R}) = \frac{c^2 t_p}{f_0 N_p T_R}$. We will explore the effect of the volume of resolution cell on the detection-tracking performance. We define and will subsequently explore a scaling factor $\sqrt{\alpha}$ which controls its volume, to $\alpha \frac{c^2 t_p}{f_0 N_p T_R}$

With respect to the third procedure it is clear for example that an LFM pulse is ill-served by a "rectangular-shaped" resolution cell better suited to CF, and vice-versa. To quantify this, we measure the uncertainty in the ambiguity function as

$$\mathbf{R}_{amb} = \frac{\int_{(r,v)} \begin{pmatrix} r \\ v \end{pmatrix} \begin{pmatrix} r \\ v \end{pmatrix}^T \mathcal{A}(r/2c, -vf_0/2c) dr dv}{\int_{(r,v)} \mathcal{A}(r/2c, -vf_0/2c) dr dv} \tag{14}$$

meaning that the ambiguity function $\mathcal{A}$ is treated as a probability density (pdf).

Assumption 4 *The resolution cell is defined as the parallelogram of a constant volume whose corners satisfy*

$$\begin{pmatrix} r \\ v \end{pmatrix}^T \mathbf{R}_{amb}^{-1} \begin{pmatrix} r \\ v \end{pmatrix} = \xi \tag{15}$$

and for which ξ is minimized.

This means, from an intuitive perspective, that were the pdf described by $\mathcal{A}$ Gaussian (it is generally not) the resolution cell as defined would maximize the enclosed probability subject to a volume constraint. The idea is illustrated in figure 6. In fact, with reference to that figure and defining

$$\mathbf{R}_{amb}^{-1} = \begin{pmatrix} \rho_{rr} & \rho_{rv} \\ \rho_{rv} & \rho_{vv} \end{pmatrix} \tag{16}$$

we have simultaneously

$$\begin{aligned} \xi &= \rho_{rr} r_1^2 + 2\rho_{rv} r_1 v_1 + \rho_{vv} v_1^2 \\ \xi &= \rho_{rr} r_2^2 + 2\rho_{rv} r_2 v_1 + \rho_{vv} v_1^2 \\ a &= 2v_1(r_1 - r_2) \end{aligned} \tag{17}$$

where a is the volume of the resolution cell ($a = \frac{c^2 t_p}{f_0 N_p T_R}$). After some algebra, we obtain

$$v_1 = \frac{\sqrt{a}}{2} \left(\frac{\rho_{rr}^2}{\rho_{rr}\rho_{vv} - \rho_{rv}^2} \right)^{1/4}$$

$$\begin{aligned} r_1 &= \frac{1}{2}\left(\frac{a}{2v_1} - \frac{2\rho_{rv}v_1}{\rho_{rr}}\right) \\ r_2 &= -\frac{1}{2}\left(\frac{a}{2v_1} + \frac{2\rho_{rv}v_1}{\rho_{rr}}\right) \end{aligned} \tag{18}$$

as the values minimizing ξ. And we finally have:

Assumption 5 *The probability of false alarm is $P_{fa} = e^{-\eta}$. The probability of a target located at (τ_a, f_a) being missed is $1 - e^{-\eta/(1+SNR\mathcal{A}(\tau_m-\tau_a, f_a-f_m))}$ for the Swerling 1 case.*

The false-alarm and miss probability expressions are reasonably well-known, and are justified in [Rago *et al.* (1998)]. The overall miss probability is again computed via the average over all (uniformly-distributed) $(r_a, v_a) \in \mathcal{R}$. Since the resolution cells are of constant volume, and are assumed to be Poisson-distributed, the Poisson parameter (average number of false alarms per unit volume) is $\lambda = \frac{P_{fa} f_0 N_p T_R}{\alpha c^2 t_p}$.

2.4 Target Motion and State Estimation

Our target model is kinematic with range/range-rate as state variables. That is, we have:

$$\mathbf{x}(\mathrm{k}+1) = \mathbf{F}\mathbf{x}(\mathrm{k}) + \mathbf{v}(\mathrm{k}) \tag{19}$$

where the process noise is white and zero-mean with covariance $E\{\mathbf{v}(\mathrm{k})\mathbf{v}^{\mathbf{T}}(\mathrm{k})\} = \mathbf{Q}$. Our observations are delay and Doppler-shift:

$$\mathbf{y}(\mathrm{k}+1) = \mathbf{H}\mathbf{x}(\mathrm{k}) + \mathbf{w}(\mathrm{k}) \tag{20}$$

where the measurement covariance $E\{\mathbf{w}(\mathrm{k})(\mathbf{w}(\mathrm{k}))^{\mathrm{T}}\} = \mathbf{R}$ is a function of the waveform shape employed. We write

$$\mathbf{F} = \begin{bmatrix} 1 & \Delta t \\ 0 & 1 \end{bmatrix} \tag{21}$$

$$\mathbf{H} = \begin{bmatrix} 2/c & 0 \\ 0 & -2f_0/c \end{bmatrix} \tag{22}$$

$$\mathbf{Q} = \sigma_{\mathrm{v}}^2 \begin{bmatrix} \frac{\Delta t^4}{4} & \frac{\Delta t^3}{2} \\ \frac{\Delta t^3}{2} & \Delta t^2 \end{bmatrix} \tag{23}$$

where Δt represents the time between samples, c is the propagation speed in the medium, f_0 is the carrier frequency, and σ_v^2 is the variance of the piecewise constant white process noise (23) [Bar-Shalom and Li (1993)]. Note that for clarity we have chosen to work in one dimension, range, since it is in this domain that the differences between the various waveform types become apparent. The *maneuvering index* $\lambda_{man} \equiv \sigma_v(\Delta t)^2/\sigma_w$ [Bar-Shalom and Li (1993)] is often used as a means of comparison of the tracking difficulty in various situations.

In the previous paper [Rago *et al.* (1998)] estimation error covariances were calculated according to a Markov chain adapted from the HYCA (hybrid conditional averaging) procedure of [Li and Bar-Shalom (1991)]. The Markov chain had two states, corresponding to a detection and missed detection at the current sample. No false alarms were assumed, and hence update could be calculated according to the Riccati equation. In this paper we allow false alarms, and assume that state estimation is via the appropriate probabilistic data association filter (PDAF) [Li and Bar-Shalom (1995)]. This implies that the full HYCA routine of [Li and Bar-Shalom (1991)] should be used; for details the reader should consult that reference.

3 Results and Discussions

Here we explore the use of two pulse trains via the analysis techniques just presented. The situation most closely corresponds to the "radar" scenario of [Rago *et al.* (1998)]; unless otherwise specified we use

- $P_{fa} = 10^{-3}$
- $\Delta t = 1$ second
- speed of propagation $c = 3 \times 10^8$ meters per second
- carrier frequency $f_0 = 4$GHz
- pulse length $t_p = 10\mu s$
- pulse repetition period $T_R = 50\mu s$
- SNR = 20dB

In the figures which follow, distance units are in meters and velocity in meters per second. Ambiguity functions are integrated once, via an FFT (fast Fourier transform) with adaptive step size, over a dense grid of range/range-rate values. For subsequent evaluations this dense grid is interpolated. In many cases (e.g. LFM, CF) there exist explicit ambiguity function expressions [Cook and Bernfeld (1993)], and these are used when appropriate.

3.1 Constant frequency (CF) pulse train

3.1.1 Effect of the sampling rate

As mentioned before, we use the factor α to control the volume of the resolution cell; that is, the sampling in time and Doppler can be scaled by a factor $\sqrt{\alpha}$, with a smaller value of α denoting finer sampling. The results are shown in figures 7, 8 and 9. From those figures, it is apparent that better performance is available when the sampling is finer. This is not surprising, considering that both measurement accuracy (bounded by the CRLB) and probability of detection (fewer misses from smaller resolution cells) are enhanced by a finer sampling. Naturally, the cost is in terms of computation, and we subsequently choose a value $\alpha = 0.17$. Further research on this topic is indicated. It is interesting that the PDAF estimation (figure 9) is of poorer quality than the measurement itself (figure 7). This is due to the relatively high miss probability and to false alarms.

3.1.2 Effect of the number of the pulses

We explore the effect of the number of pulses N_p, in figures 10, 11, and 12. Please note that overall signal to noise ratio is kept constant, meaning that the amplitude of each pulse is proportional to $1/\sqrt{N_p}$. From figure 10 it is clear that measurement error decreases with an increasing number of pulses, explainable from the increased centrality of the ambiguity function. The trend is not uniform, as an even number of pulses offers superior performance to odd, presumably an artifact of a relatively "busy" ambiguity function. It is noteworthy that the decrease appears to reach a limit. Observe further from figure 11 that the miss probability rises with the number of pulses for the same reason. These two effects do not precisely offset: it appears from figure 12 that the overall tracking error is decreased by a greater number of pulses, particularly and not-unexpectedly in velocity.

3.2 Linear frequency modulated (LFM) pulse train

3.2.1 Effect of correlation

The results for an LFM pulse train having $t_p = 10\mu s,\ T_R = 50\mu s$ are shown in figures 13, 14, and 15; and for $t_p = 1\mu s,\ T_R = 5\mu s$ in figures 16, 17, and 18. In terms of *measurement* quality (figures 13 and 16) there is no difference between downsweep (negative sweep rate) and upsweep. However, as is clear from figures 14 and 17 the correlation between range and range-rate measurements is positive in the former and negative in the latter.

The dependable superiority of LFM *up*sweep, as opposed to LFM downsweep or CF, previously reported in [Daum (1992), Rago *et al.* (1998), Niu *et al.* (1999)], is we hope clear from figures 15 and 18. Further, it is seen that the sensitivity to the choice of waveform *decreases* as the target becomes more agile (higher σ_v). The reason for the former is, of course, that the estimation error for a kinematic target tends to exhibit positive correlation between position and velocity; if this is treated as *prior* information, then overall accuracy is enhanced by a measurement having complementary characteristics, meaning an LFM upsweep with its *negatively*-correlated position and velocity measurements. As to the latter, consider that a larger σ_q corresponds to prior information of lower quality (higher motion uncertainty). With poorer prior localization the tracking system is forced to rely more heavily on each measurement as it becomes available: as is suggested by figure the measurement accuracy (meaning the size of the diagonal terms in its correlation matrix) has more to do with the pulse length that waveform. This is illustrated in figure 26.

3.2.2 Effect of envelope shading

In [Niu *et al.* (1999)] it was observed that Hamming and/or Gaussian shading (i.e. windowing) of the transmitted pulse [Cook and Bernfeld (1993)] had a beneficial effect on tracking in the single-pulse sonar situation, due to the more manageable sidelobe behavior. For the former we use

$$s_n(t) \quad = \quad \begin{cases} [0.08 + 0.92\cos^2\frac{\pi(t-\frac{T}{2})}{T}]e^{jbt^2} & 0 \le t < T \\ 0 & else \end{cases} \tag{24}$$

and the ambiguity function is given in figure 19. Figures 20-25 correspond to earlier figures 13-18. The situation is less clear in this radar-parametrized situation than for sonar, and indeed it appears that the rectangular shading is somewhat preferable. This may be due to the increased sampling effort ($\alpha = .17$) in use here.

3.2.3 Effect of the sweep rate

It is clear that sweep rate affects tracking performance, and moreover that this effect is itself a function of the target's process noise level. There is usually a "best" (always positive) LFM sweep rate to use for a particular target dynamic model; the intuition behind this is given in figure 27.

Further, this best sweep rate decreases as the maneuvering index increases. This is an indication that for low-maneuvering targets the orientation of the prior (tracking error) covariance ellipse becomes more horizontal (again see figure 27); an alternative way of putting this is that for such a target velocity is well-estimated and reasonably unchanging, and the improved position measurements from a high sweep rate are most desirable. A higher sweep rate confers greater posterior accuracy on position measurements, and lesser on velocity measurements. This

is valuable when the velocity varies slowly (low λ_{man}); if velocity varies rapidly (high λ_{man}), then the enhanced accuracy in velocity measurement of a low sweep-rate is more appropriate.

This is explored quantitatively in figures 28 and 29, in which the optimal sweep rate is determined as a function of maneuvering index. Note that a shorter pulse requires a higher sweep rate in order to that the same frequency excursion be obtained; it is interesting that the total frequency excursion required for best performance with a shorter pulse length is actually greater than for a longer pulse.

3.2.4 Effect of measurement model

Assumption 2 earlier stipulated that when a number of near or contiguous resolution cells enjoyed "hits", then the measurement supplied to the tracker is taken as their average, as illustrated in figure 5. We are aware that this is perhaps oversimplified, in that some amplitude weighting may be useful, or indeed that some morphological or image-processing techniques may be used. The procedures appear to be in many cases proprietary and unavailable for general comment. In this section we mention a simple alternative to the direct "averaging" scheme to which it can be compared. The idea is that (12,13) are replaced by

$$\begin{aligned}&(\hat{r}(\gamma, r_a, v_a), \hat{v}(\gamma, r_a, v_a)) \\ &\quad = \quad \text{argmax}_{(r_m, v_m)} \{\mathcal{A}(\tau_m - \tau_a, f_a - f_m) \text{ such that } \gamma \mathcal{A}(\tau_m - \tau_a, f_a - f_m) \geq \eta\} \end{aligned} \tag{25}$$

and this may be thought of as a "strongest-neighbor" approach, although the correspondence is not exact. From figures 30-32 it is apparent that this new scheme is inferior to the original. Presumably the averaging approach yields sub-cell accuracy, which by and large the new scheme does not.

3.3 Alternating CF and LFM pulses

In [Niu *et al.* (1999)] it was observed that a 50%-50% *combined* CF/LFM pulse could in some situations produce superior performance. Such a combined pulse was essentially an abutment of two half-duration pulses, with assumed coherence. In the current situation it appears that the same effect can be obtained via alternation of pulses: LFM followed by CF followed by LFM, etc. We explore this idea in figures 33-35, plotted as a function of sweep rate for those pulses which are LFM. It turns out that although the measurements themselves appear to be superior in this case to pure LFM (see figure 33), their resolution cells are essentially rectangular (see figure 34), and hence there is no beneficial effect to be had from upsweep LFM's negative correlation between range and range-rate measurements see figure 35). In fact, there is a slight tendency for *up*sweep LFM to produce a *positive* correlation and hence results degraded with respect to downsweep, presumably from sidelobe structure; but this effect is minimal.

4 Summary

In this paper we have investigated the effect on tracking performance of the type of waveform used. Measurements of a one-dimensional kinematic target are assumed derived from sampling a two-dimensional (range and range-rate) grid of points whose locations are fixed, meaning that the target's true location need not coincide with these points. As such, a key concept is the resolution cell from which these sampling points are derived, and we have taken for this the parallelogram of constant volume whose orientation most closely matches that of the implied

ambiguity function. The results are analytical, and are based on the HYCA tracking performance prediction algorithm for the PDAF – false alarms are included in a natural way.

This paper extends the sonar-parameter results in [Niu *et al.* (1999)] to the radar situation; in doing so, it is necessary to allow for coherent processing of multi-pulse waveforms. Of particular interest is the necessity for restriction of attention to the main ambiguity function peak from amongst the usual "bed of nails". We list the following:

- As before, LFM *up*sweep is relatively difficult to beat, due largely to its negative correlation between range and range-rate measurements.
- It is possible to specify an optimal LFM sweep rate as a function of target maneuvering index.
- Sampling on a finer time-frequency grid yields uniformly better performance. Thus, sampling effort must be traded against computational effort.
- Unlike the sonar situation, there does not appear to be benefit from Hamming shading of the transmitted pulses.
- As the number of pulses being integrated increases tracking performance improves. While this may appear obvious, note that the statement is made about a system whose overall SNR is held fixed, meaning that more pulses corresponds to lower amplitude on each.
- An alternating LFM/CF pulse scheme does not appear to offer any tangible benefits.
- In [Niu *et al.* (1999)] a key assumption was that the measurement supplied to the tracker was the *average* of local threshold exceedances. For the most part that assumption was used in this paper, but also tested was a scheme whereby only the *strongest* return was supplied. It turned out that this was a poor idea: the sub-cell accuracy of the original idea was lost.

The conclusion that upsweep LFM is heartening, in that it corroborates much radar practice.

Acknowledgement

This research has been supported by ONR/BMDIO-IST under contract number N00014-91-J-1950, by AFOSR under contract number F49620-95-1-0299, and by ONR under contract number N00014-97-1-0502.

References

[Daum (1992)] F. Daum, "A System Approach to Multiple Target Tracking", *Multitarget-Multisensor Tracking: Applications and Advances*, volume II, Y. Bar-Shalom ed, pp149-181. Artech House, 1992.

[Kershaw and Evans (1997)] D. Kershaw and R. Evans, "Waveform Selective Probabilistic Data Association", *IEEE Transaction on Aerospace and Electronic Systems*, pp1180-1188, October 1997.

[Rago *et al.* (1998)] C. Rago, P. Willett and Y. Bar-Shalom, "Detection-Tracking Performance with Combined FM-CW Waveforms", *IEEE Transaction on Aerospace and Electronic Systems*, vol 34, pp612-624, April 1998.

[Niu *et al.* (1999)] R. Niu, P. Willett, and Y. Bar-Shalom, "From the Waveform through the Resolution Cell to the Tracker", *Proceedings of the 1999 Aerospace Conference*, Snowmass CO, March 1999.

[Levanon (1988)] Nadav Levanon *Radar Principles*, Wiley, 1988.

[Bar-Shalom and Li (1993)] Y. Bar-Shalom and X. Li, *Estimation and Tracking: Principles, Techniques and Software*, Artech House, 1993.

[Scheer and Kurtz (1993)] I. Scheer and J. Kurtz, *Coherent Radar Performance Estimation*, Artech House, 1993.

[Li and Bar-Shalom (1991)] X. Li and Y. Bar-Shalom, "Stability Evaluation and Track Life of the PDAF for Tracking in Clutter", *IEEE Transactions on Automatic Control*, pp588-602, May 1991.

[Li and Bar-Shalom (1995)] Y. Bar-Shalom and X. Li, *Multisensor, Multitarget Tracking: Principles and Techniques*, YBS Publishing, 1995.

[Cook and Bernfeld (1993)] C. Cook and M. Bernfeld, *Radar Signals: An Introduction to Theory and Application*, Artech House, 1993.

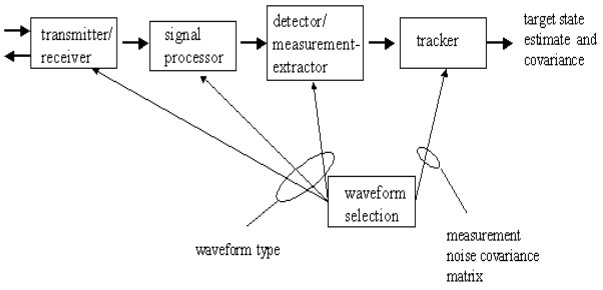

Figure 1: System block diagram: the waveform is selected and this choice must be shared with all subsystems up to the tracker. The information provided to the tracker should be of the measurements' locations, and also of their associated covariances, which depend on the waveform.

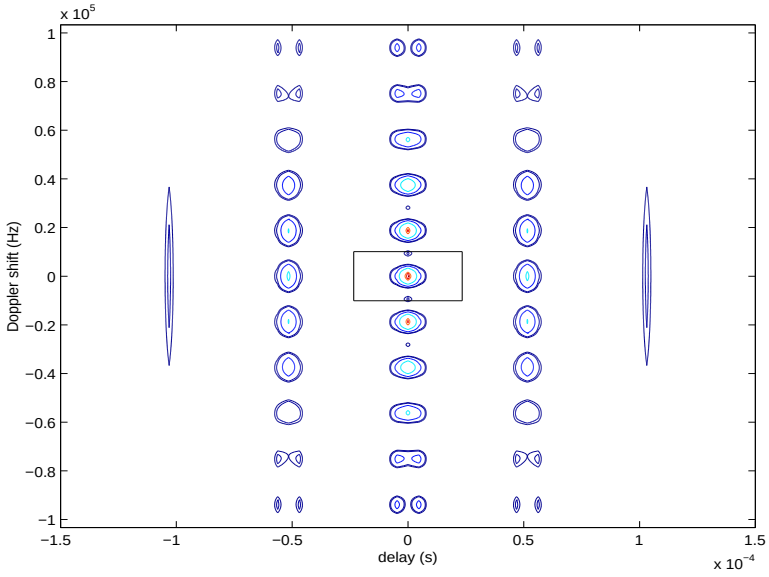

Figure 2: The ambiguity function contours and the neighborhood region around the main peak for a CF pulse train, $t_p = 10\mu s$, $T_R = 50\mu s$, $N_p = 3$.

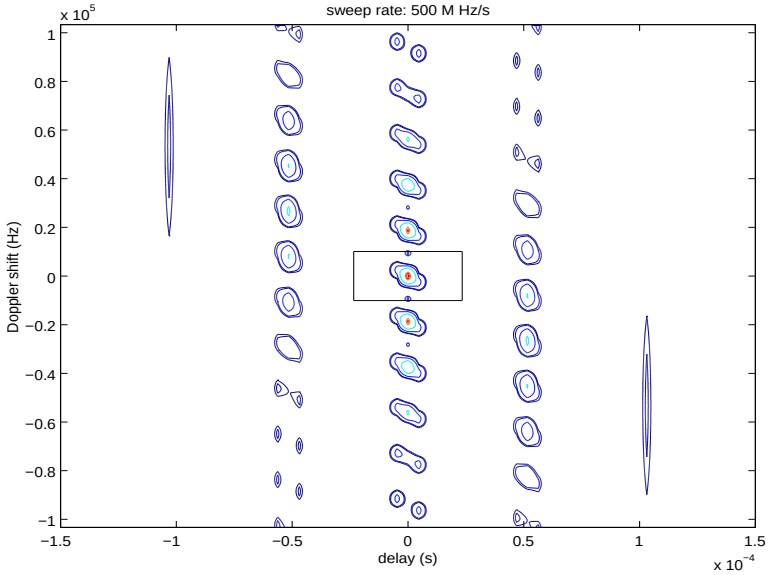

Figure 3: The ambiguity function contours and the neighborhood region around the main peak for a LFM pulse train, $t_p = 10\mu s$, $T_R = 50\mu s$, $N_p = 3$, and sweep rate $5 \times 10^8 Hz/s$.

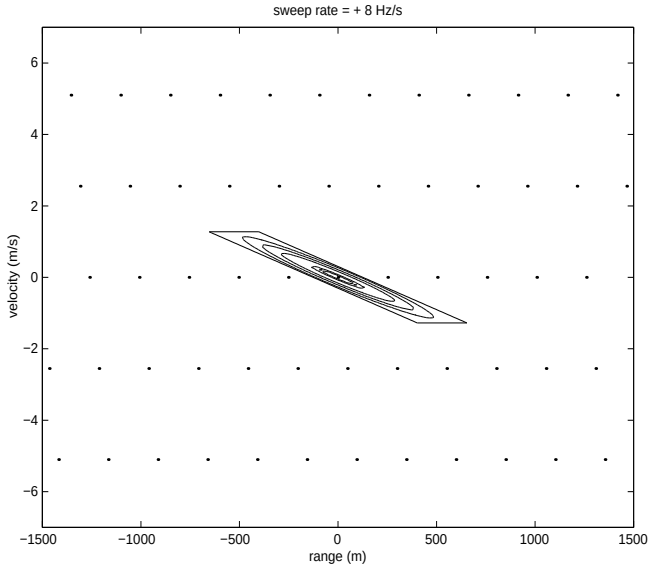

Figure 4: The resolution cell (parallelogram), ambiguity function contours and $\{(r_m, v_m)\}$ sampling points (dots) for an LFM waveform.

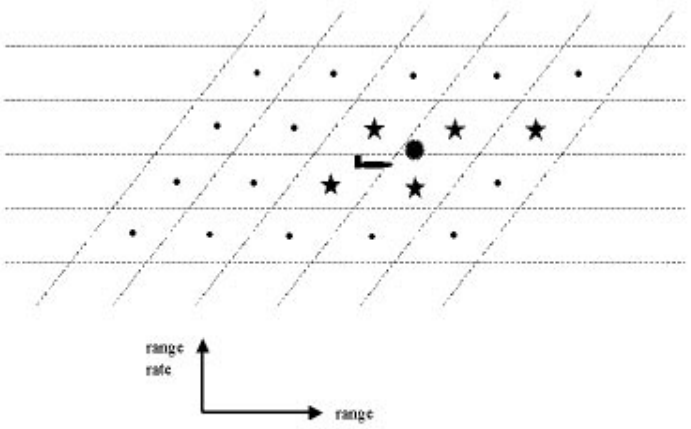

Figure 5: Illustration of derivation of measurement delivered to tracker. The target's position, denoted by an airframe shape, is not at the center of a resolution cell – resolution cells are parallelograms, and their center's denoted by ∘'s. The threshold exceedances are shown as five-pointed stars, and their average (the delivered measurement) as a many-pointed star.

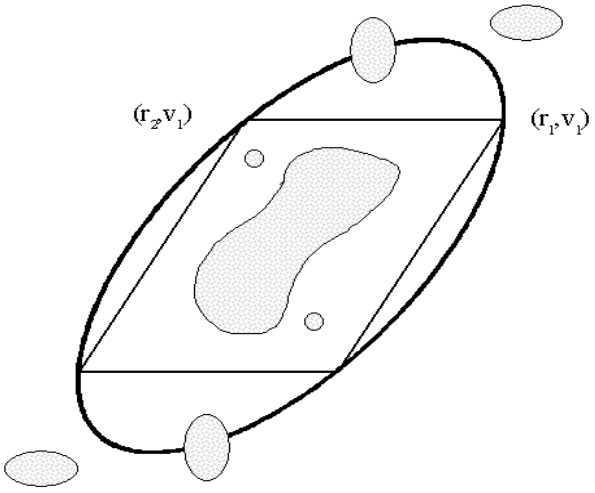

Figure 6: Illustration of the procedure of finding the resolution cell. The shaded region denotes range/range-rate values within an ambiguity function contour. From this the ambiguity function uncertainty $\mathbf{R}_{amb}$ is formed, and is pictured as the ellipse. The actual resolution cell is drawn within that ellipse.

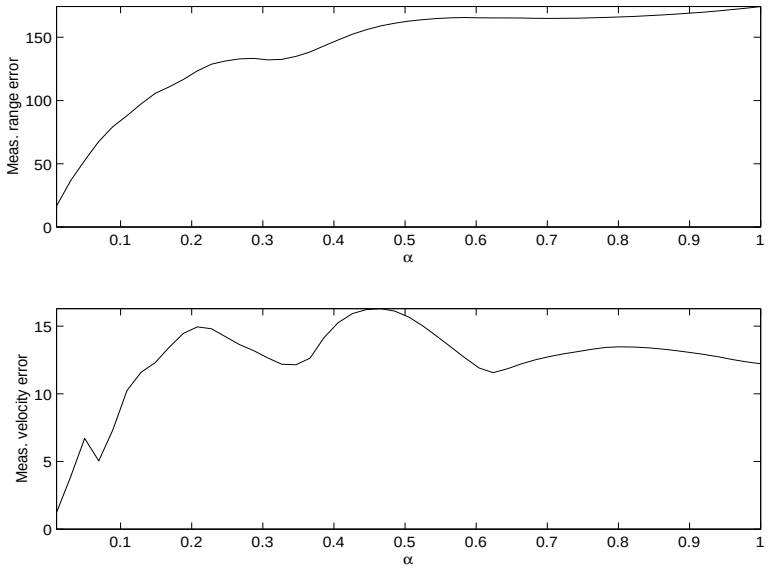

Figure 7: Measurement range and range-rate error as a function of α for a rectangular-shaded CF pulse train, $N_p = 20$

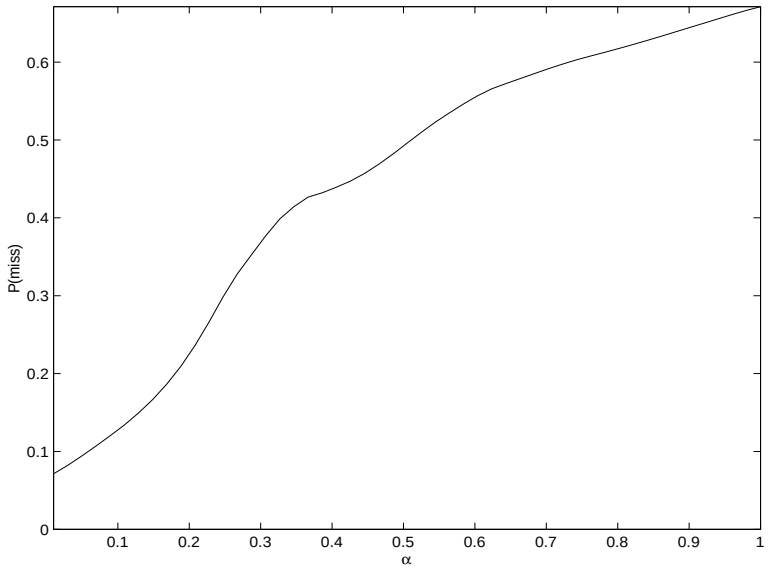

Figure 8: Probability of miss as a function of α for a rectangular-shaded CF pulse train, $N_p = 20$

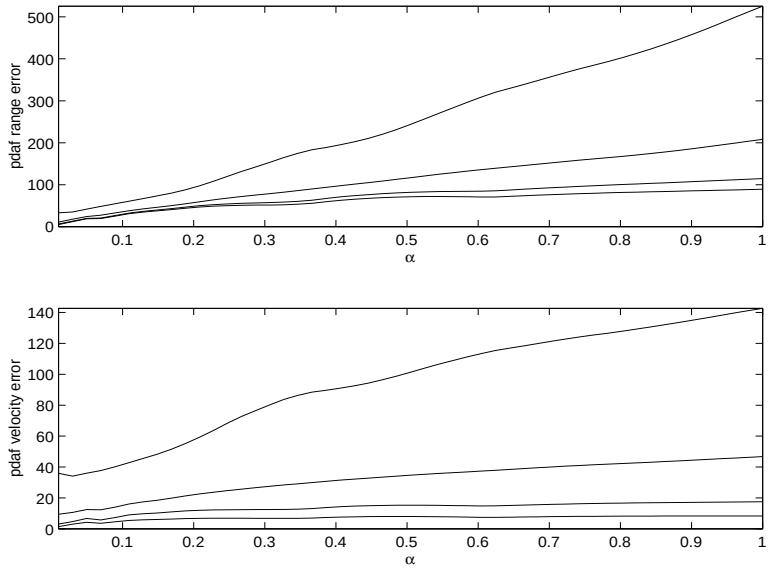

Figure 9: Measurement range and range-rate error as a function of α for a rectangular-shaded CF pulse train , $N_p = 20$. In each figure, bottom, middle, and top curves refer to $\sigma_v^2 = 10, 100, 1000, 10000$, corresponding to maneuvering indices $\lambda_{man} = .0073, .023, .073, .23$, respectively.

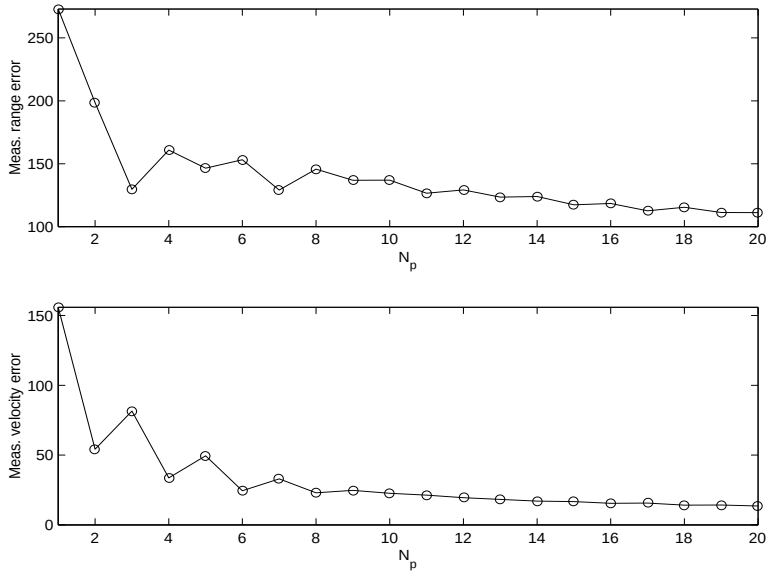

Figure 10: Estimation range and range-rate error as a function of N_p for a uniform pulse train, $\alpha = 0.17$

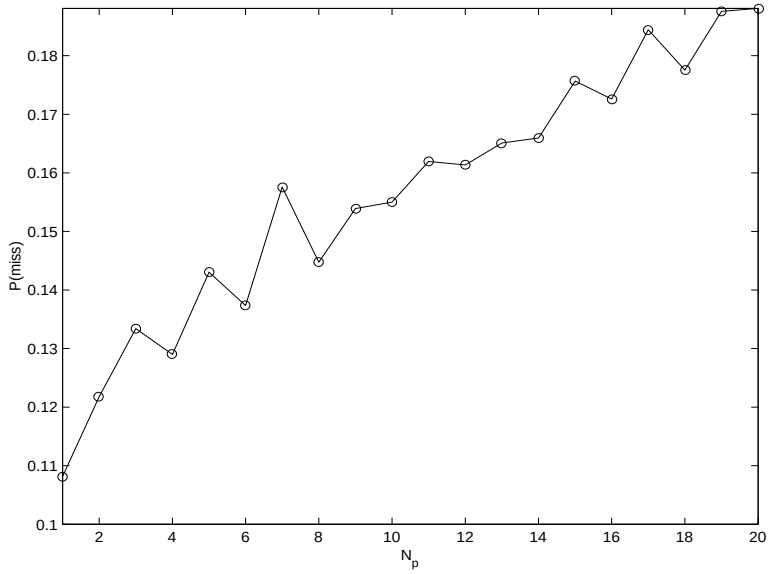

Figure 11: Probability of miss as a function of N_p for a uniform pulse train, $\alpha = 0.17$

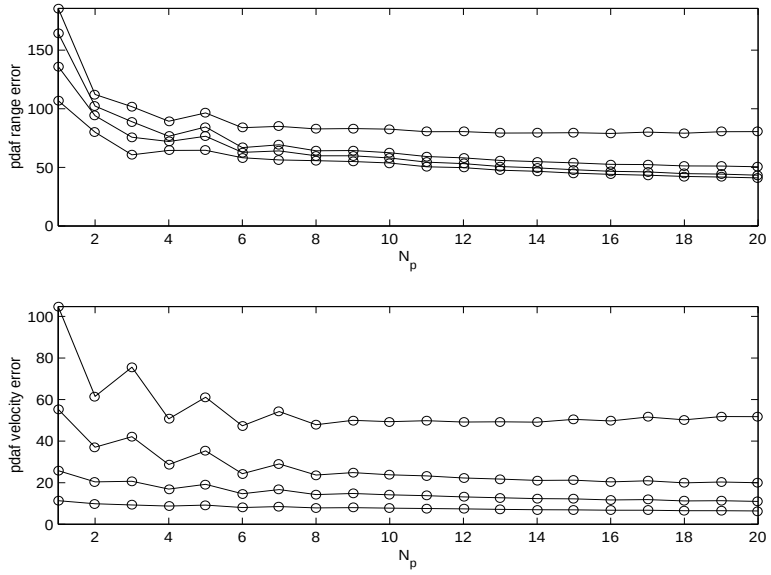

Figure 12: Estimation range and range-rate error as a function of N_p for a uniform pulse train, $\alpha = 0.17$. In each figure, bottom, middle, and top curves refer to $\sigma_v^2 = 10, 100, 1000, 10000$, corresponding to maneuvering indices $\lambda_{man} = .0073, .023, .073, .23$, respectively.

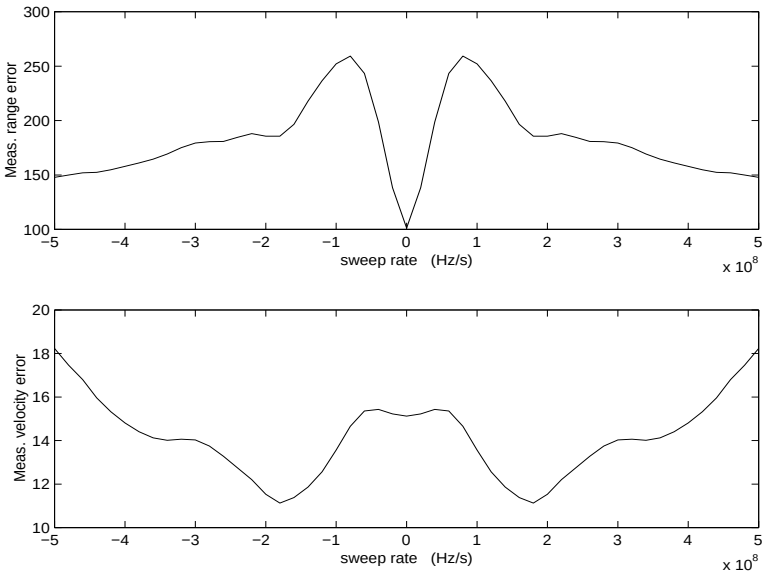

Figure 13: Measurement range and range-rate error as a function of sweep rate for a LFM pulse train, $\alpha = 0.17$ and $N_p = 20$.

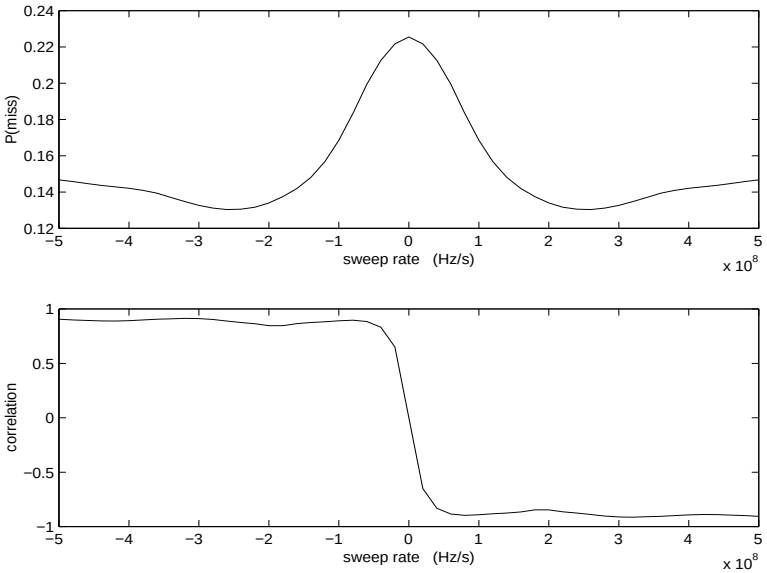

Figure 14: Probability of miss as a function of sweep rate for a LFM pulse train, $\alpha = 0.17$ and $N_p = 20$.

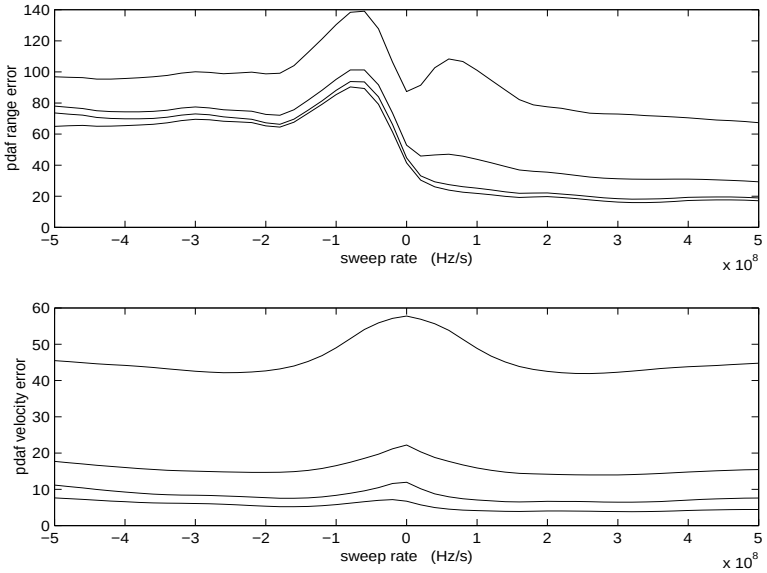

Figure 15: Estimation range and range-rate error as a function of sweep rate for a LFM pulse train, $\alpha = 0.17$ and $N_p = 20$. In each figure, bottom, middle, and top curves refer to $\sigma_v^2 = 10, 100, 1000, 10000$.

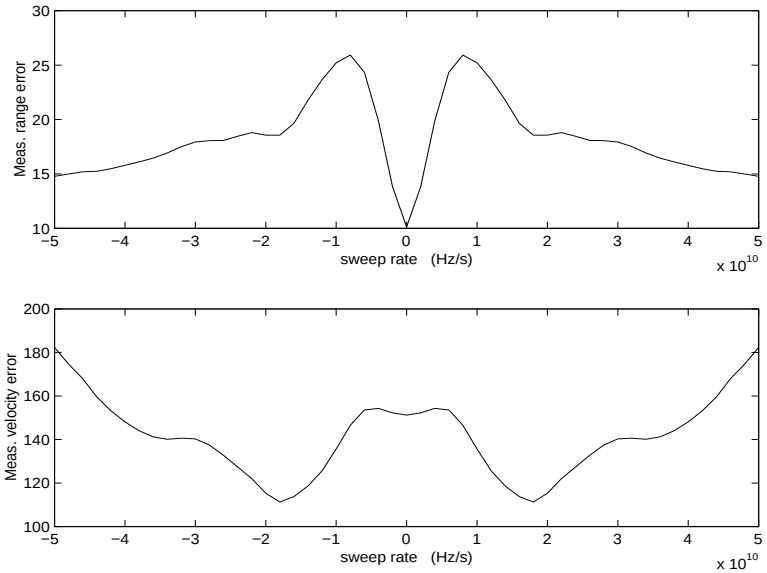

Figure 16: Measurement range and range-rate error as a function of sweep rate for a LFM pulse train, $\alpha = 0.17,\ N_p = 20,\ t_p = 1\mu s,\ T_R = 5\mu s$.

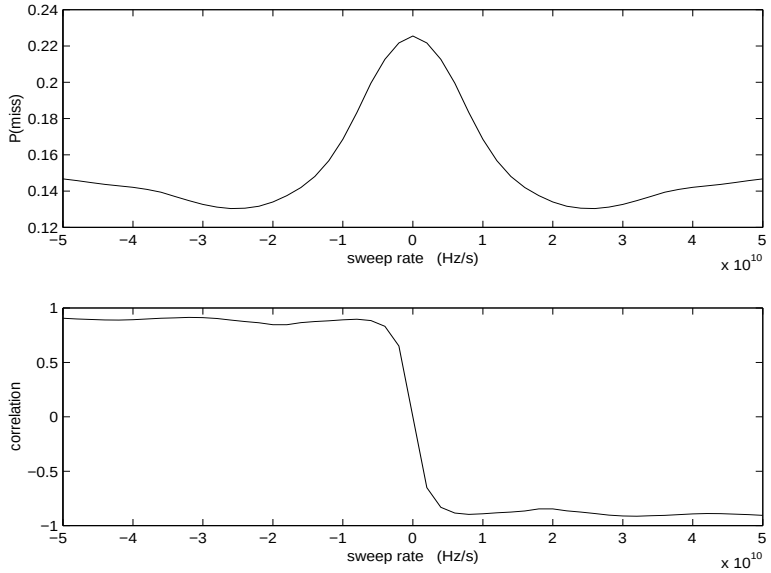

Figure 17: Probability of miss as a function of sweep rate for a LFM pulse train, $\alpha = 0.17,\ N_p = 20,\ t_p = 1\mu s,\ T_R = 5\mu s$.

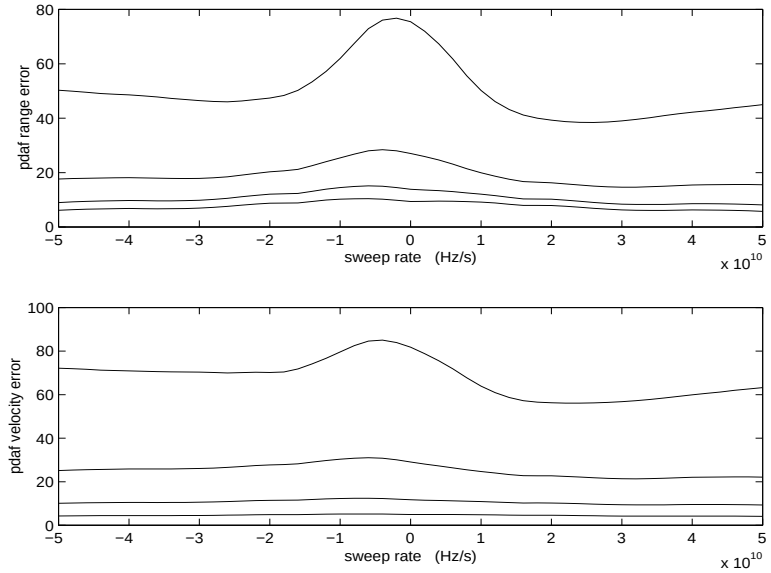

Figure 18: Estimation range and range-rate error as a function of sweep rate for a LFM pulse train, $\alpha = 0.17,\ N_p = 20,\ t_p = 1\mu s,\ T_R = 5\mu s$. In each figure, bottom, middle, and top curves refer to $\sigma_v^2 = 10, 100, 1000, 10000$, corresponding to maneuvering indices $\lambda_{man} = .073, .23, .73, 2.3$, respectively.

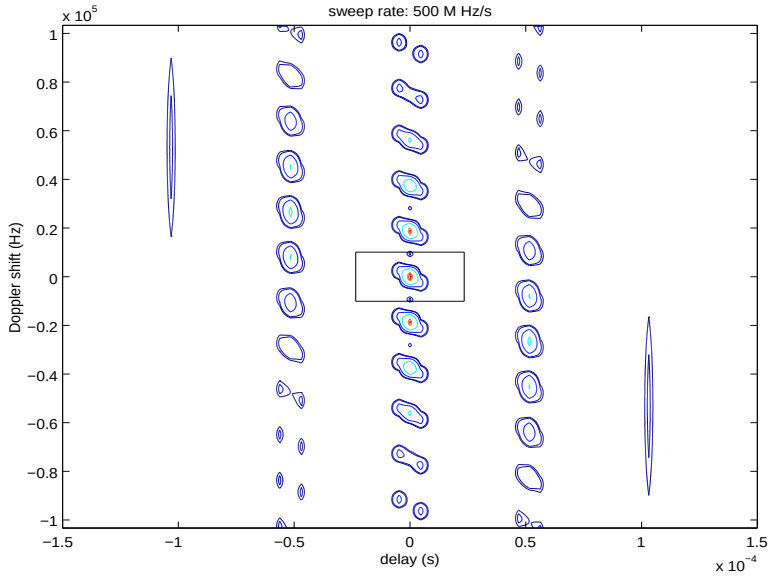

Figure 19: The ambiguity function contours and the neighborhood region around the main peak for a Hamming shaded CF pulse train, $t_p = 10\mu s$, $T_R = 50\mu s$, $N_p = 3$, and sweep rate $5 \times 10^8 Hz/s$.

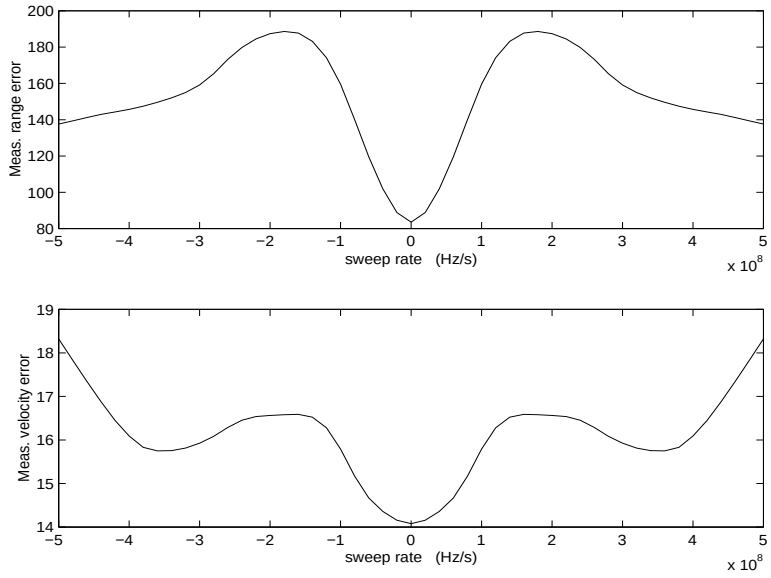

Figure 20: Measurement range and range-rate error as a function of sweep rate for a Hamming shaded LFM pulse train, $\alpha = 0.17$ and $N_p = 20$.

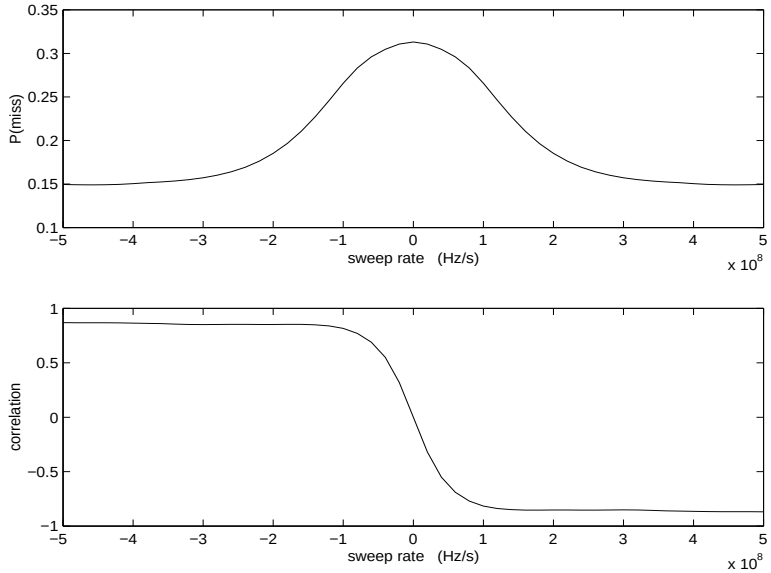

Figure 21: Probability of miss as a function of sweep rate for a Hamming shaded LFM pulse train, $\alpha = 0.17$ and $N_p = 20$.

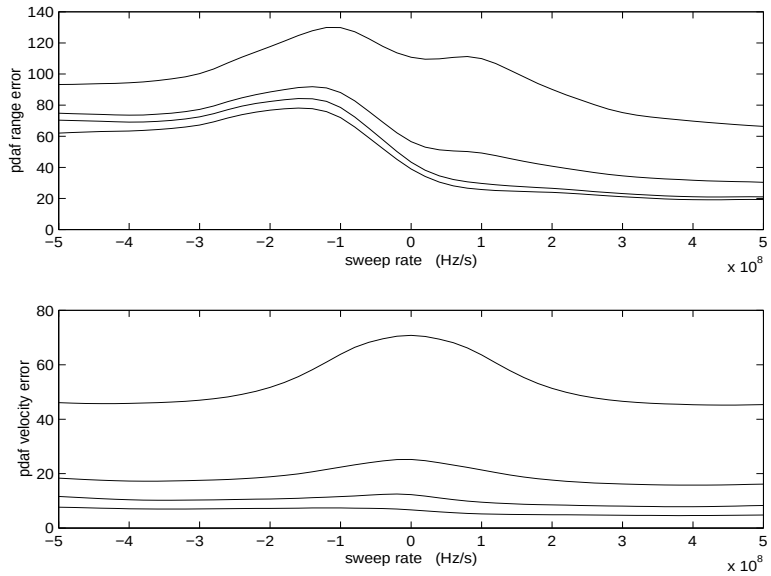

Figure 22: Estimation range and range-rate error as a function of sweep rate for a Hamming shaded LFM pulse train, $\alpha = 0.17$ and $N_p = 20$. In each figure, bottom, middle, and top curves refer to $\sigma_v^2 = 10, 100, 1000, 10000$, corresponding to maneuvering indices $\lambda_{man} = .0073, .023, .073, .23$, respectively.

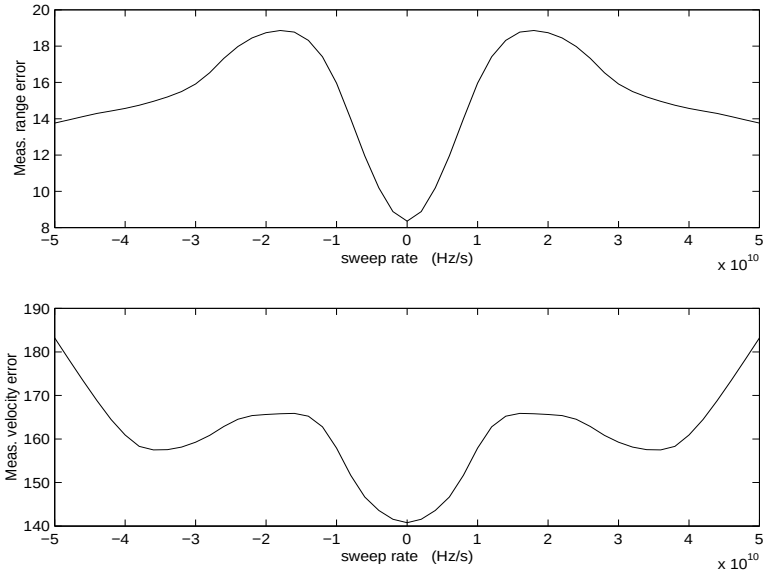

Figure 23: Measurement range and range-rate error as a function of sweep rate for a Hamming shaded LFM pulse train, $\alpha = 0.17,\ N_p = 20,\ t_p = 1\mu s,\ T_R = 5\mu s$.

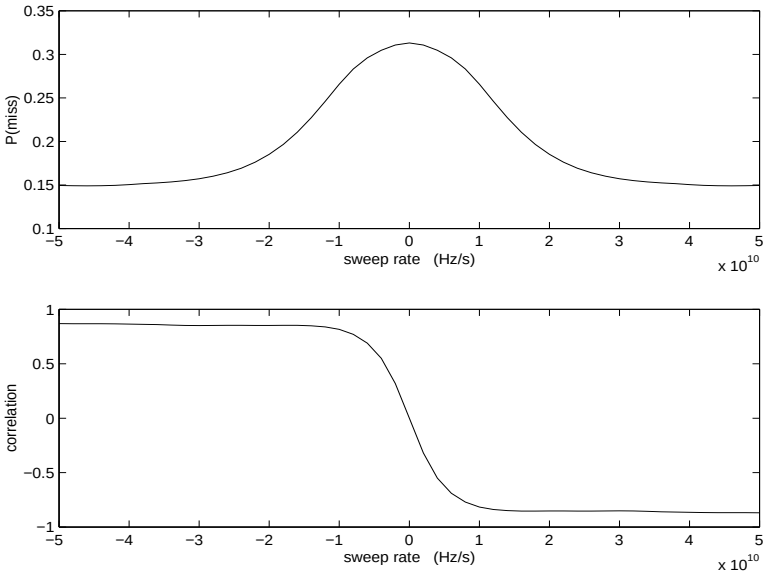

Figure 24: Probability of miss as a function of sweep rate for a Hamming shaded LFM pulse train, $\alpha = 0.17,\ N_p = 20,\ t_p = 1\mu s,\ T_R = 5\mu s$.

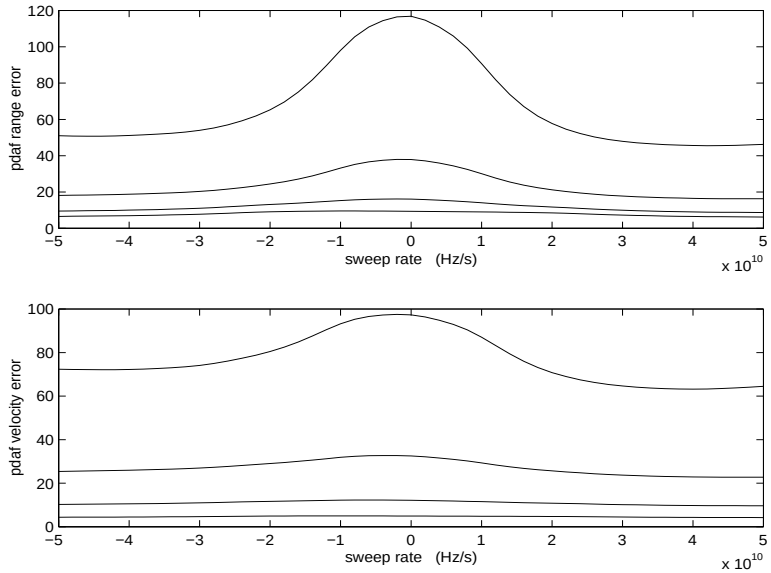

Figure 25: Estimation range and range-rate error as a function of sweep rate for a Hamming shaded LFM pulse train , $\alpha = 0.17,\ N_p = 20,\ t_p = 1\mu s,\ T_R = 5\mu s$. In each figure, bottom, middle, and top curves refer to $\sigma_v^2 = 10, 100, 1000, 10000$, corresponding to maneuvering indices $\lambda_{man} = .073, .23, .73, 2.3$, respectively.

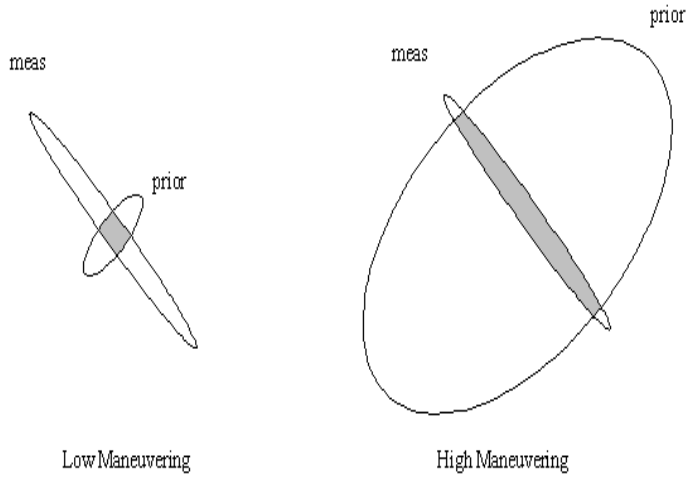

Figure 26: Heuristics of combination of prior (tracking) and posterior (measurement) information. On the left the prior information is of high quality (small σ_q), and hence its combination with the measurement, as represented by the shaded intersection region, is better than either alone. On the right σ_q is large, and the intersection as projected on either axis is little smaller than for the measurement alone.

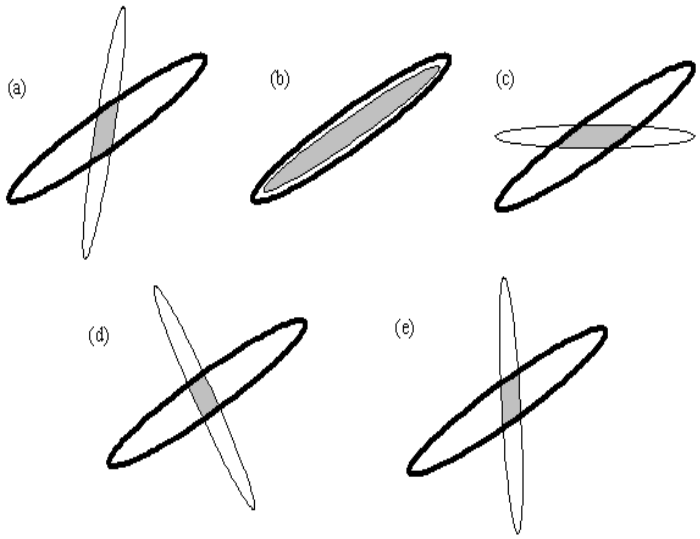

Figure 27: Heuristics of the effect of different sweep rates on tracking performance. (a) High negative sweep rate, hence tracking performance as illustrated by intersection between prior and measurement correlation ellipses, is good; (b) Negative sweep rate is such that orientation between prior and measurement ellipses is the same – the worst LFM waveform to use; (c) CF situation; (d) Positive LFM sweep, best LFM waveform; (e) LFM upsweep rate is too high, some enlargement of posterior uncertainty over (d).

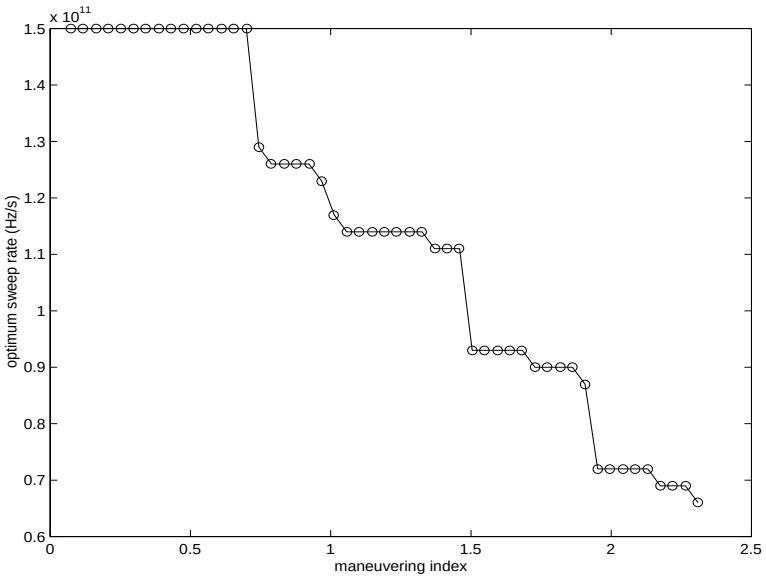

Figure 28: Optimal LFM sweep rates for $N_p = 10$, $t_p = 1\mu s$, and $T_R = 5\mu s$, plotted as a function of maneuvering index. Note that a 100GHz/s sweep rate corresponds to a total frequency excursion of 100kHz.

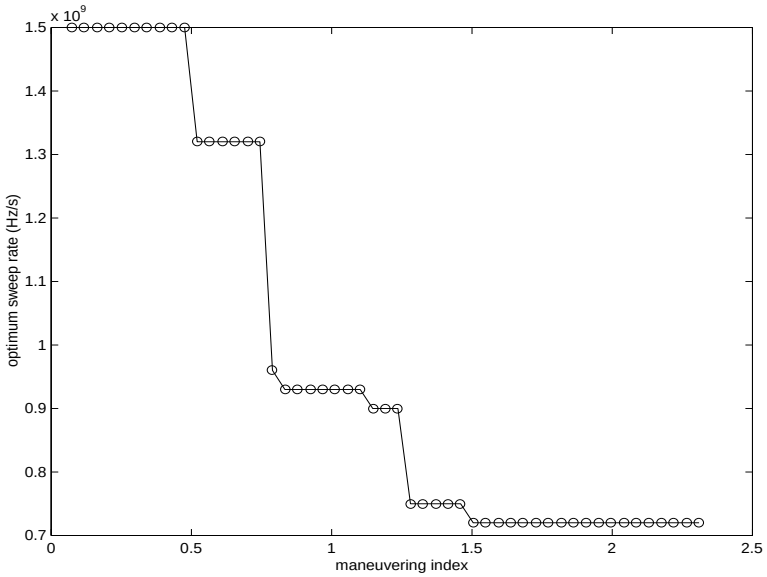

Figure 29: Optimal LFM sweep rates for $N_p = 10$, $t_p = 10\mu s$, and $T_R = 50\mu s$, plotted as a function of maneuvering index. Note that a 1GHz/s sweep rate corresponds to a total frequency excursion of 10kHz.

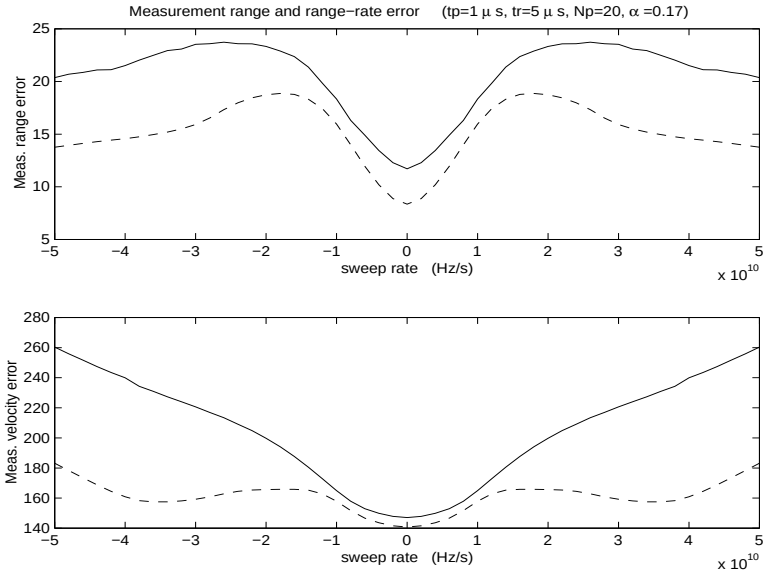

Figure 30: Measurement range and range-rate error as a function of sweep rate for a LFM pulse train, $\alpha = 0.17$, $N_p = 20$, $t_p = 1\mu s$, $T_R = 5\mu s$. The dashed line is for the original "averaging" measurement model of (12,13); that for the solid line is the new "strongest-neighbor"-like measurement model of (25).

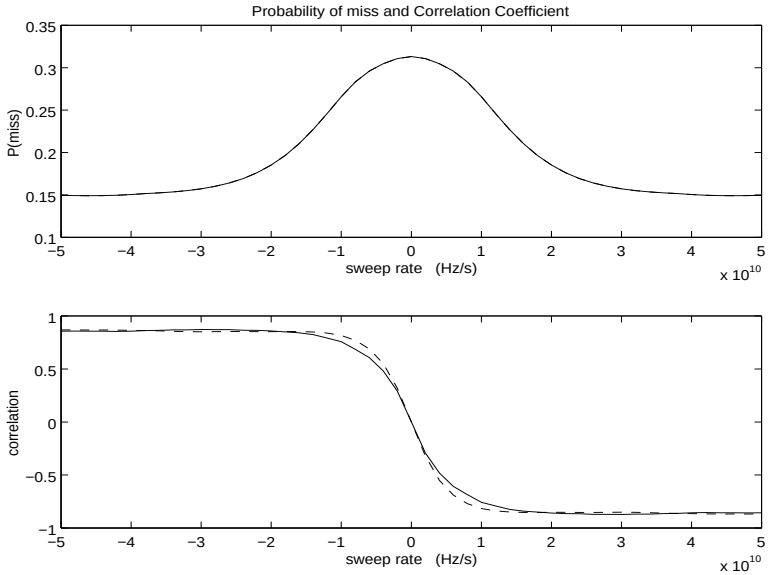

Figure 31: Probability of miss as a function of sweep rate for a Hamming shaded LFM pulse train, $\alpha = 0.17,\ N_p = 20,\ t_p = 1\mu s,\ T_R = 5\mu s$. The dashed line is for the original "averaging" measurement model of (12,13); that for the solid line is the new "strongest-neighbor"-like measurement model of (25).

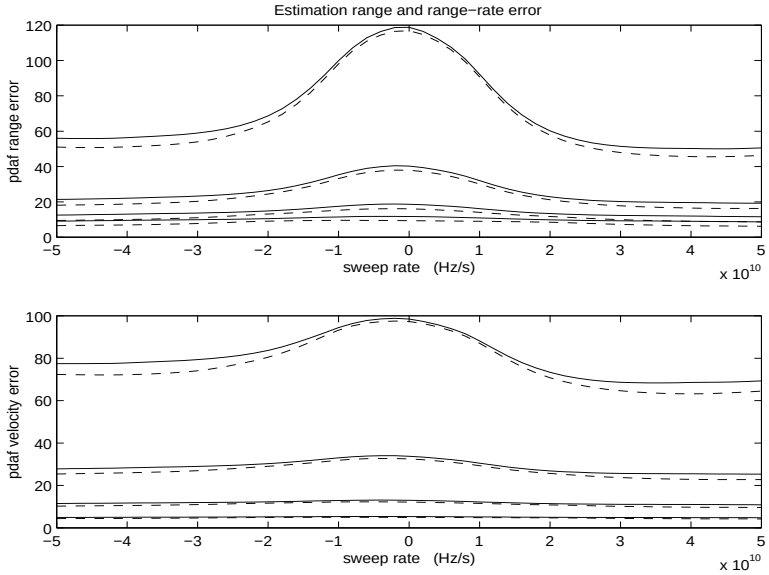

Figure 32: Estimation range and range-rate error as a function of sweep rate for a Hamming shaded LFM pulse train , $\alpha = 0.17,\ N_p = 20,\ t_p = 1\mu s,\ T_R = 5\mu s$. In each figure, bottom, middle, and top curves refer to $\sigma_v^2 = 10, 100, 1000, 10000$, corresponding to maneuvering indices $\lambda_{man} = .073, .23, .73, 2.3$, respectively. The dashed line is for the original "averaging" measurement model of (12,13); that for the solid line is the new "strongest-neighbor"-like measurement model of (25).

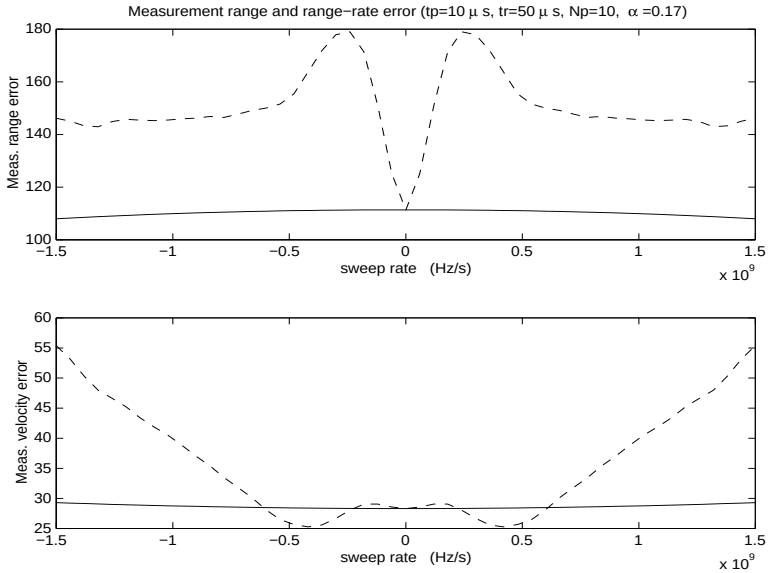

Figure 33: Measurement range and range-rate error as a function of sweep rate for a LFM pulse train, $\alpha = 0.17,\ N_p = 10,\ t_p = 10\mu s,\ T_R = 50\mu s$. The dashed line refers to standard LFM pulses, and the solid to alternating LFM/CF pulses.

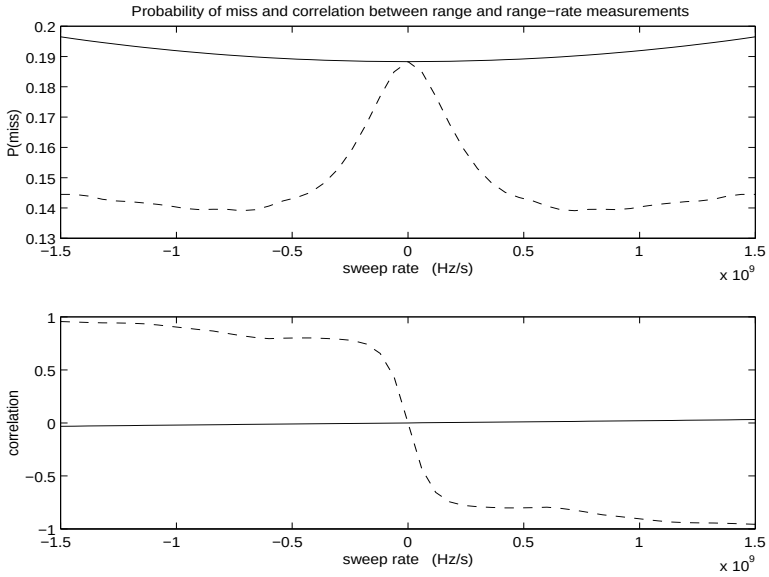

Figure 34: Probability of miss and correlation coefficient as a function of sweep rate for a Hamming shaded LFM pulse train, $\alpha = 0.17,\ N_p = 10,\ t_p = 10\mu s,\ T_R = 50\mu s$. The dashed line refers to standard LFM pulses, and the solid to alternating LFM/CF pulses.

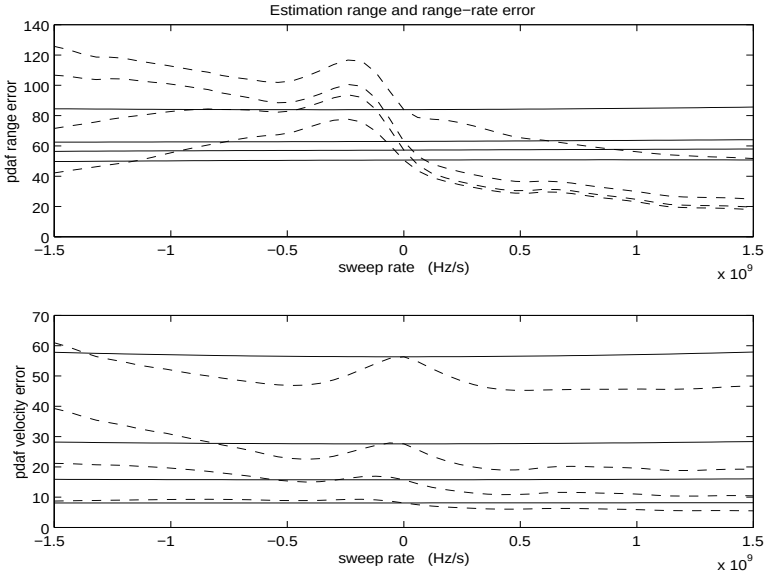

Figure 35: Estimation range and range-rate error as a function of sweep rate for a Hamming shaded LFM pulse train , $\alpha = 0.17,\ N_p = 10,\ t_p = 10\mu s,\ T_R = 50\mu s$. In each figure, bottom, middle, and top curves refer to $\sigma_v^2 = 10, 100, 1000, 10000$, corresponding to maneuvering indices $\lambda_{man} = .0073, .023, .073, .23$, respectively. The dashed line refers to standard LFM pulses, and the solid to alternating LFM/CF pulses.